PHOTONICS Research

Free-space local nonseparability dynamics of vector modes

Xiao-Bo Hu,[1] Benjamin Perez-Garcia,[2,5] Valeria Rodríguez-Fajardo,[3] Raul I. Hernandez-Aranda,[2] Andrew Forbes,[3] and Carmelo Rosales-Guzmán[1,4,*]

[1]Wang Da-Heng Collaborative Innovation Center, Heilongjiang Provincial Key Laboratory of Quantum Manipulation and Control, Harbin University of Science and Technology, Harbin 150080, China
[2]Photonics and Mathematical Optics Group, Tecnologico de Monterrey, Monterrey 64849, Mexico
[3]School of Physics, University of the Witwatersrand, Johannesburg 2050, South Africa
[4]Centro de Investigaciones en Óptica, A.C., Loma del Bosque 115, Colonia Lomas del campestre, 37150 León, Gto., Mexico
[5]e-mail: b.pegar@tec.mx
*Corresponding author: carmelorosalesg@cio.mx

Received 30 November 2020; revised 26 January 2021; accepted 27 January 2021; posted 29 January 2021 (Doc. ID 416342); published 15 March 2021

One of the most prominent features of quantum entanglement is its invariability under local unitary transformations, which implies that the degree of entanglement or nonseparability remains constant during free-space propagation, true for both quantum and classically entangled modes. Here we demonstrate an exception to this rule using a carefully engineered vectorial light field, and we study its nonseparability dynamics upon free-space propagation. We show that the local nonseparability between the spatial and polarization degrees of freedom dramatically decays to zero while preserving the purity of the state and hence the global nonseparability. We show this by numerical simulations and corroborate it experimentally. Our results evince novel properties of classically entangled modes and point to the need for new measures of nonseparability for such vectorial fields, while paving the way for novel applications for customized structured light.

https://doi.org/10.1364/PRJ.416342

1. INTRODUCTION

It is well known that entanglement is invariant to local unitary transformations. An example of such is the well-known fact that the degree of entanglement remains unmodified upon free-space propagation. Crucially, nonseparability, the fundamental aspect of entanglement, is not exclusive to quantum systems, and this principle applies to both nonlocal and local entanglement at the single- and multiphoton levels. The former is observed between photons that simultaneously exist in physically separated locations, and the latter between the internal degrees of freedom of photons. Classical states of light such as complex vectorial light fields [1] also exhibit local entanglement, attributed to the nonseparability between their spatial and polarization degrees of freedom (DoFs). Here it is worth clarifying what is meant by such a statement, and to this end we follow the terminology of several seminal works [2–5]. The definition of entanglement is simply the nonseparability of sums of product states that exist in different vector spaces. While there are many options for the DoFs to use with optical fields, e.g., spatial, temporal, frequency, mode index, and even more exotic choices such as path and trajectory [6], here we are interested in the vector spaces made of the polarization and spatial modes, defined by our two DoFs, the former two dimensional and the latter infinite dimensional. The resulting Hilbert space describing the field is the tensor product of the two, i.e., an infinite number of two-dimensional spaces. We will consider the dynamics of one pure state vector in such a Hilbert space. We adopt conventional notation in the literature and call this state a "vector beam" if the polarization is nonhomogeneously distributed in space and a "scalar beam" if homogeneously distributed. Our interest here is in the former: vector beams nonseparable in the polarization and spatial mode DoFs, controversially called "classically entangled" [5,7–9]. Despite the controversy, it is becoming clear that some quantum systems can be tested and probed with classically entangled light [10–12]. For example, classical entanglement has been exploited in quantum error correction [13], quantum state tomography [14], optical communications [15–17], and optical metrology [18–20]. Additionally, the tightly focusing properties of complex vector modes have been exploited in the field of optical tweezers [21–27], micromachining [28], as well as in super-resolution microscopy [29–31].

Recently, there has been an increasing interest in the engineering of vector light beams whose polarization state varies upon free-space propagation. Most of these have focused on the generation of pure vector beams that oscillate from one vec-

tor state to another while keeping a constant degree of nonseparability [32–37]. A more interesting case, which encloses the previous cases, reported the generation of light beams whose degree of nonseparability oscillates between scalar and vector modes, offering a tool for the on-demand delivery of specific states to desired positions [38]. Such oscillating modes are generated from the superposition of two counterpropagating vector beams, whose implementation can be cumbersome. While these studies have only considered cylindrical vector vortex modes, the use of new symmetries (spatial shapes), such as parabolic or elliptical, could potentially allow us to unveil properties of vector modes that up to now have remained hidden.

Here we demonstrate a new class of vector beam whose degree of nonseparability features interesting dynamics as it propagates, evolving from a nonhomogeneously polarized vector beam to a quasi-homogeneously polarized beam. Such modes are generated from a nonseparable superposition of orthogonal parabolic beams, which are natural solutions to the Helmholtz equation in parabolic cylindrical coordinates [39–44], and orthogonal polarization states. The entanglement dynamics are quantified through a modified measurement of concurrence C, commonly used to measure the degree of nonseparability in vector modes [45–49]. It is noteworthy that, while it is tempting to view these beams as separable in their two degrees of freedom, vindicated by the local measure of C, their global concurrence remains unchanged.

2. THEORETICAL BACKGROUND

The concept presented in this paper is schematically shown in Fig. 1. At the generation plane ($z = 0$), the parabolic vector beam possesses a maximum degree of nonseparability, clearly evinced as a nonhomogeneous polarization distribution, overlapped with the intensity profile of the vector mode. Upon propagation, the polarization structure of the beam evolves from completely mixed and locally nonseparable to completely unmixed and locally separable, the latter reached in the far field ($z = \infty$).

The engineered vector beams are constructed from a superposition of traveling parabolic-Gaussian (TPG$^{\pm}$) beams. Mathematically, TPG beams are given by superposition of the even and odd parabolic-Gaussian (PG) beams as [39]

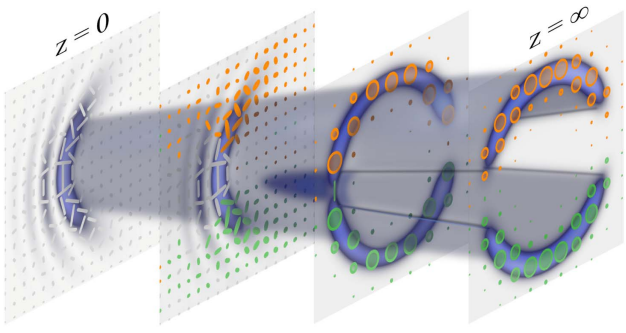

Fig. 1. Schematic representation of a classically entangled light mode featuring a separation of both degrees of freedom upon free space propagation. Right and left circular polarizations are represented by orange and green ellipses, while linear polarization is represented by gray lines.

$$\mathrm{TPG}^{\pm}(\mathbf{r};a) = \mathrm{PG}^{e}(\mathbf{r};a) \pm i\mathrm{PG}^{o}(\mathbf{r};a). \tag{1}$$

Here the functions $\mathrm{PG}^{e,o}(\cdot)$ are the even and odd PG modes of the parabolic cylindrical coordinates $\mathbf{r} = (\eta, \xi, z)$, given by [44]

$$\mathrm{PG}^{e}(\mathbf{r};a) = \exp\left(-i\frac{k_t^2}{2k}\frac{z}{\mu}\right)\mathrm{GB}(\mathbf{r})\frac{|\Gamma_1|^2}{\pi\sqrt{2}}P_e\left(\sqrt{\frac{2k_t}{\mu}}\xi;a\right) \times P_e\left(\sqrt{\frac{2k_t}{\mu}}\eta;-a\right), \tag{2}$$

$$\mathrm{PG}^{o}(\mathbf{r};a) = \exp\left(-i\frac{k_t^2}{2k}\frac{z}{\mu}\right)\mathrm{GB}(\mathbf{r})\frac{2|\Gamma_3|^2}{\pi\sqrt{2}}P_o\left(\sqrt{\frac{2k_t}{\mu}}\xi;a\right) \times P_o\left(\sqrt{\frac{2k_t}{\mu}}\eta;-a\right),$$

where $P_e(\cdot)$ and $P_o(\cdot)$ are the even and odd solutions of the parabolic cylindrical differential equation $[d^2/dx^2 + (x^2/4 - a)]P(x;a) = 0$, and $a \in (-\infty, \infty)$ represents the continuous order of the beam. Importantly, the solutions $P_e(\cdot)$ and $P_o(\cdot)$ can be written in terms of Kummer confluent hypergeometric functions [50], which are available in many numerical libraries. Furthermore, $\Gamma_1 = \Gamma[(1/4) + (1/2)ia]$ and $\Gamma_3 = \Gamma[(3/4) + (1/2)ia]$, with $\Gamma(\cdot)$ the gamma function; and k_t is the transverse component of the wave vector $\mathbf{k}$, whose magnitude is related to the longitudinal component k_z as $k^2 = k_t^2 + k_z^2$. Additionally, $\mathrm{GB}(\mathbf{r})$ is the fundamental Gaussian beam given by

$$\mathrm{GB}(\mathbf{r}) = \frac{\exp(ikz)}{\mu}\exp\left(-\frac{r^2}{\mu\omega_0^2}\right), \tag{3}$$

where $\mu = \mu(z) = 1 + iz/z_r$ with $z_r = k\omega_0^2/2$ being the usual Rayleigh range of a Gaussian beam. The parabolic coordinates $\mathbf{r} = (\eta, \xi, z)$ are related to the Cartesian coordinates as $x = (\eta^2 - \xi^2)/2$ and $y = \eta\xi$, where $\eta \in [0, \infty)$ and $\xi \in (-\infty, \infty)$. For values $\gamma = k_t\omega_o \gg 1$, the PG beam propagates in a nondiffracting way within the range $[-z_{\max}, z_{\max}]$, where $z_{\max} = \omega_0 k/k_t$.

The traveling parabolic-Gaussian vector (TPGV) beams are generated as a nonseparable weighted superposition of the polarization and spatial degrees of freedom. Here the polarization degree of freedom is encoded in the circular polarization basis while the spatial degree of freedom is precisely encoded in the TPG$^{\pm}(\cdot)$ modes. Mathematically, such superposition can be written as

$$\mathrm{TPGV}(\mathbf{r};a) = \frac{1}{\sqrt{2}}[\mathrm{TPG}^{+}(\mathbf{r};a)\hat{e}_R + \mathrm{TPG}^{-}(\mathbf{r};a)\exp(i\phi)\hat{e}_L], \tag{4}$$

where the unitary vectors $\hat{e}_R$ and $\hat{e}_L$ represent the right and left circular states of polarization, respectively. Finally, the term $\exp(i\phi)$ ($\phi \in [-\pi/4, \pi/4]$) is a phase difference between both constituting modes.

An example of such a superposition is schematically illustrated in Fig. 2 using the modes $\mathrm{TPG}^{+}(\mathbf{r};3)$ and $\mathrm{TPG}^{-}(\mathbf{r};3)$,

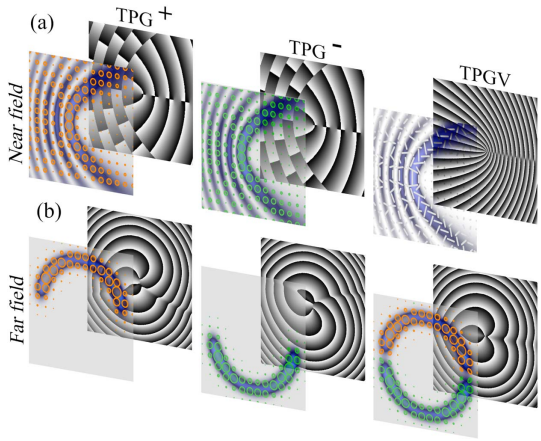

Fig. 2. Phase (back panels) and polarization distribution overlapped with the intensity profiles (front panels) of the scalar modes $\mathrm{TPG}^{+}(\mathbf{r};a)\hat{e}_R$ (left) and $\mathrm{TPG}^{-}(\mathbf{r};a)\hat{e}_L$ (middle), which are combined to generate the TPGV mode (right) at the (a) near and (b) far field. In the case of the TPGV mode, we depict the phase of the complex Stokes field $S = S_1 + iS_2$.

where the back panels show the phase distribution, whereas the front ones show the intensity profile overlapped with the corresponding polarization distribution. In Fig. 2(a), we present the near field of each individual component (left and middle panels) as well as the complex superposition (right panel), and in Fig. 2(b) we show their corresponding far-field counterparts. Notice the difference between the near field, completely mixed and locally nonseparable, and the far field, completely unmixed and locally separable.

3. EXPERIMENTAL GENERATION OF TPGV MODES

A schematic representation of our experimental setup for generate arbitrary vector modes is depicted in Fig. 3(a). A horizontally polarized laser beam ($\lambda = 532$ nm) is expanded and collimated by lenses L_1 and L_2, and subsequently transformed into a diagonally polarized beam by use of a half-wave plate (HWP) at 22.5°. A polarizing beam splitter (PBS) separates the beam into its horizontal and vertical polarization components. Both beams are then directed, one with the help of a mirror (M), to a polarization-insensitive digital micromirror device (DMD, DLP Light Crafter 6500 from Texas Instruments), impinging under slightly different angles (≈1.5°) at the center of the DMD. Here there is a multiplexed hologram consisting of the superposition of two independent holograms with unique linear phase gratings, each corresponding to the constituting wave fields of Eq. (4), TPG^{+} and TPG^{-} modes. Additional details about the generation and multiplexing of the holograms can be found in Refs. [46,51–53]. In this way, the period of the grating is used to ensure the first diffraction order of each beam to propagate along a common axis, where the vector beam is generated. Once generated, a spatial filter (SF) placed at the focusing point of a telescope composed by lenses L_3 and L_4 removes all higher diffraction orders. A quarter-wave plate (QWP_1) is added to change the TPG mode from the linear $(\hat{e}_H, \hat{e}_V)$ to the circular polarization basis $(\hat{e}_L, \hat{e}_R)$. In order to reach the far field, a long focal distance lens L_5 ($f = 300$ mm) was inserted in the path of the beam. The use of a long focal distance lens is crucial to avoid well-known polarization effects caused by strong focusing, which allow us to neglect the polarization component of the field along the propagation direction. Finally, a charge-coupled device (CCD; FL3-U3-120S3C-C with a resolution of 4000×3000 pixels and a pixel size of 1.55 μm) mounted on a rail parallel to the propagation direction of the beam was used to record the intensity of the beam.

To quantify the degree of nonseparability we relied on a well-known measure from quantum mechanics, the concurrence C, which assigns a value in the range [0,1] to the degree of entanglement [45–49]. The concurrence C is measured by integrating the Stokes parameters $S_i, i = 0, 1, 2, 3$ over the entire transverse plane through the relation [46,47]

$$C = \sqrt{1 - \left(\frac{\mathbb{S}_1}{\mathbb{S}_0}\right)^2 - \left(\frac{\mathbb{S}_2}{\mathbb{S}_0}\right)^2 - \left(\frac{\mathbb{S}_3}{\mathbb{S}_0}\right)^2}, \tag{5}$$

where $\mathbb{S}_i = \iint_{R^2} S_i \mathrm{d}A$. The Stokes parameters S_i are computed from a set of four intensity measurements as [54]

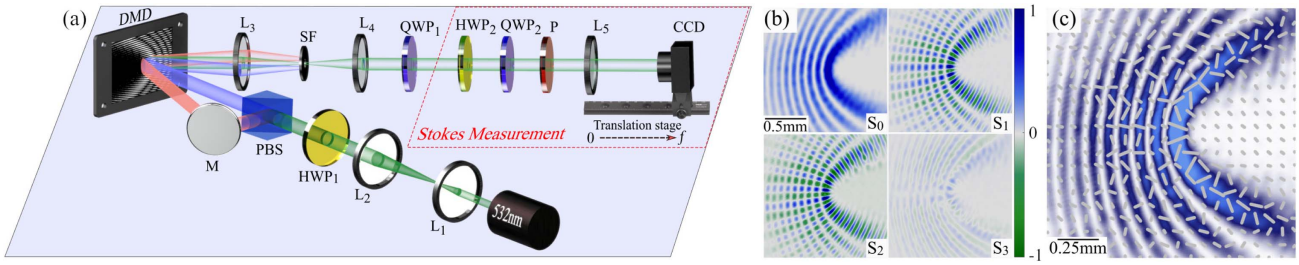

Fig. 3. (a) To experimentally generate the TPGV mode, we used a novel approach based on a digital micromirror device (DMD). A laser beam expanded and collimated (by lenses L_1 and L_2) is diagonally polarized with a half-wave plate (HWP_1) and split by a polarizing beam splitter (PBS) according to its polarization components. The two beams are redirected to the DMD, impinging at slightly different angles but overlapped at the center of a binary multiplexed hologram where the TPG^{+} and TPG^{-} scalar modes are encoded, each with a unique linear grating. After the DMD, the first diffraction order of each beam overlaps along a common propagation axis where the TPGV is generated. A spatial filter (SF) placed at the focusing plane of a telescope formed by lenses L_3 and L_4 removes all higher diffraction orders. A quarter-wave plate (QWP_1) transforms the mode from the linear to the circular polarization basis. The nonseparability dynamics are quantified through Stokes polarimetry, for which a set of four intensities are recorded with a charge-coupled device (CCD) camera. (b) Experimental Stokes parameters S_1, S_2, and S_3 of the TPGV mode $\mathrm{TPGV}(\mathbf{r}, 3)$. (c) Intensity profile overlapped with the reconstructed polarization distribution.

$$S_0 = I_0, \quad S_1 = 2I_H - S_0,$$
$$S_2 = 2I_D - S_0, \quad S_3 = 2I_R - S_0, \tag{6}$$

where I_0 is the total intensity of the mode and I_H, I_D, and I_R the intensity of the horizontal, diagonal, and right-handed polarization components, respectively. As illustrated in Fig. 3(a), such intensity measurements were acquired by a CCD camera through the combination of a linear polarizer (P) and a quarter-wave plate (QWP_2) [55]. Specifically, the intensities of the horizontal (I_H) and diagonal (I_D) polarization components were obtained by passing the beam through a linear polarizer at 0° and 45°, respectively, whereas intensity corresponding to the RCP component (I_R) was obtained by passing the beam simultaneously through a QWP at 45° and a linear polarizer at 90°. As an example, Fig. 3(b) shows the experimental Stokes parameters S_0, S_1, S_2, and S_3 for the specific mode TPGV($\mathbf{r}$, 3) at $z = 0$. Such parameters were used to reconstruct the transverse polarization distribution on a 20 × 20 grid as shown in Fig. 3(c). Here, for the sake of clarity, we also display the transverse intensity profile. For this specific example, we have $\mathbb{S}_1/\mathbb{S}_0 = 0.12$, $\mathbb{S}_2/\mathbb{S}_0 = 0.09$, and $\mathbb{S}_3/\mathbb{S}_0 = -0.02$, which upon substitution in Eq. (5) yield the value $C = 0.98$, which, as expected, corresponds to a maximally entangled mode.

4. ANALYSIS OF THE NONSEPARABILITY DYNAMICS

In this section, we present a detailed analysis of the propagation dynamics of our TPGV beams. This analysis is performed experimentally and through numerical simulations using the Rayleigh–Sommerfeld diffraction theory [56]. As a first evidence of the evolution dynamics, we reconstructed the polarization distribution at various transverse planes. A representative set of results are displayed in Fig. 4(a) for the case TPGV($\mathbf{r}$; 3) for $\omega_0 = 2$ mm and $k_t = 22.5$ mm^{-1}, for which $z_{\max} = 1050$ mm. Here the transverse intensity profile is shown overlapped with its corresponding polarization distribution at four different planes, namely, $z = 0$, $z = 1.2z_{\max}$, $z = 3.0z_{\max}$, and $z = \infty$. Experimentally, these distances correspond to the values $z' = 243$ mm, $z' = 274$ mm, and $z' = f$, obtained through the well-known equation of a thin lens, $1/z + 1/z' = 1/f$. As shown, the plane $z = 0$ features a vector mode with a nonhomogeneous polarization distribution. For $z > 0$, the beam evolves from completely mixed and locally nonseparable to completely unmixed and locally separable, featuring a smooth transition from linear to circular polarization. For comparison, in Fig. 4(b) we show the theoretical counterparts, where the same behavior is observed. It is worth mentioning that the demagnification of the beam as a function of propagation considerably reduces the number of pixels forming the beam's intensity, which could in principle affect the resolution of the reconstructed polarization. Nonetheless, the use of a high-resolution CCD (in our case a CCD camera with 1.55 μm pixel size) ensures that even at the focal plane we have enough pixels for a proper reconstruction. In addition, for a better comparison between experiment and numerical simulations, we used identical spatial resolutions. Note that the focusing experimental beam acquires an elliptical shape, which

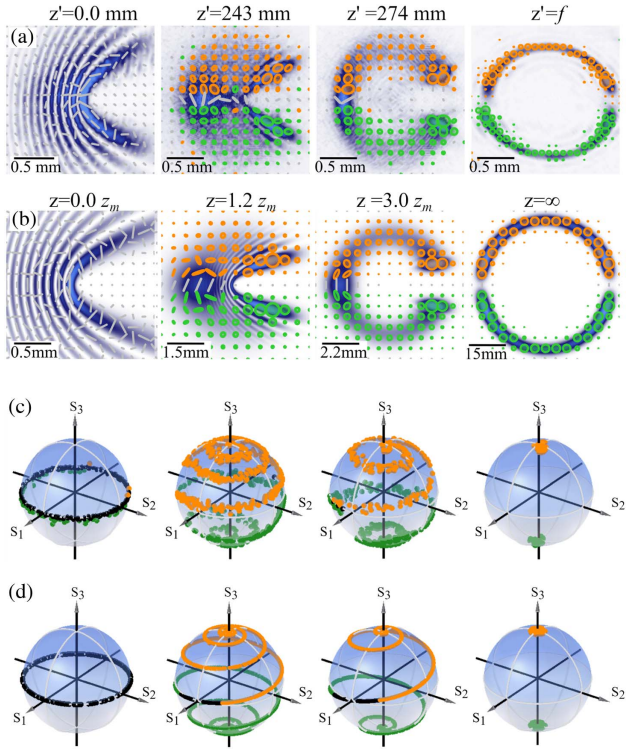

Fig. 4. (a) Experimental and (b) simulated evolution of intensity and polarization distribution of TPGV beams as a function of propagation distance. (c) Experimental and (d) simulated representation of the transverse polarization distribution on a Poincaré sphere, each in correspondence with the planes shown in (a) and (b).

results from optical aberrations caused by the nonhomogeneous flattening of the DMD's screen, which can be corrected as explained in Ref. [57].

With the idea of better visualizing the evolution of polarization upon propagation, we mapped the different states of polarization acquired at each plane onto the well-known Poincaré sphere (PS), in which the different polarization states are associated to unique points on the surface of the sphere [54] as shown in Figs. 4(c) and 4(d) for experiment and numerical simulation, respectively. Here the coordinate axes are given in terms of the Stokes parameters S_1, S_2, and S_3. For $z = 0$, all the states of polarization in the transverse plane are linear and therefore mapped to points along the equator. For $z > 0$, such linear polarization states gradually evolve from linear into elliptical and finally to circular. In the PS, this is seen as points along a spiral trajectory connecting the north and south poles, in the intermediate planes, and in the far field as points on the north and south poles. Notice that even though the polarization structure evolves from completely mixed to completely unmixed, the amount of right- and left-elliptically polarized photons remains in equilibrium.

One way to quantify the nonseparability dynamics of the TPGV modes, as a function of the propagation distance z [Eq. (5)], is through the computation of the concurrence C. Nonetheless, the concurrence of the whole beam, which we call global concurrence, yields $C \approx 1$ for every propagation plane. The reason being, as mentioned before, the amount of left- and

right-elliptically polarized photons is always the same regardless of the propagation distance. Hence, even though locally all the Stokes parameters might have nonzero values, globally S_1, S_2, and S_3 will be always zero, resulting in $\mathbb{S}_i = \iint_{R^2} S_i dA = 0$ for $i = 1, 2, 3$, which implies $C = 1$ for all values of z. This implies that the global concurrence fails to account for the changes in the polarization distribution that are observed in Fig. 4. This can be illustrated by computing a local concurrence C_L, i.e., the concurrence of small sections of the beam, across the entire transverse plane and at different propagation distances. This is shown in Fig. 5(a), where we performed a numerical simulation of C_L along the vertical direction across the beam and as a function of the propagation distance. Here, for each $z \in [0, 4z_{\max}]$, we sectioned the beam from top to bottom into 50 rectangular regions (2 mm × 40 μm each) and computed the concurrence on each of them. As can be seen, for short propagation distances $z \approx 0$, the concurrence stays closer to one for all beam positions, which is expected since at the origin plane both degrees of freedom are completely mixed over the full transverse plane. Figure 5(b) shows an example of the area over which C was computed for the specific case $z = 0$. This area corresponds to the solid line shown in Fig. 5, which illustrates a decay of C as a function of z. Notice that in the center of the beam C remains constant regardless of the propagation distance. To further understand this, in Fig. 5(c) we show the integration area for this particular position at $z = 3z_{\max}$, which clearly shows that even though in this region both polarization states are completely separated, it contains the same amount of right- and left-elliptically polarized photons, yielding $C = 1$. The corresponding concurrence as a function of the propagation area for this section is shown as a dashed line in Fig. 5. In addition to the simulation, in this figure we also present experimental values of the concurrence for the cases $z/z_{\max} = 0, 0.2, 0.7, 1.3, 2.2$, and 3.6, shown as points over the 3D surface, which agree very well with the simulation. Figure 5 clearly evinces that local concurrence is the appropriate measure to quantify the decay in the degree of local nonseparability, even

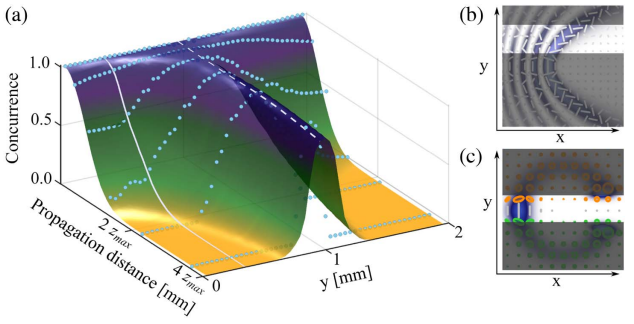

Fig. 5. (a) Concurrence as a function of propagation and transverse coordinates. The solid and dashed lines show two examples of C as a function of z for the specific sections of the beam, shown in (b) and (c), which correspond to $z = 0$ and $z = 4z_{\max}$, respectively. The surface corresponds to numerical simulations and the data points to experimental measurements at the propagation planes $z/z_{\max} = 0, 0.2, 0.7, 1.3, 2.2$, and 3.6. An analogous behavior has been reported in the context of temporal coherence [58], where the generation of beams whose local degree of temporal coherence varies as a function of the time difference is discussed.

though it fails in the center of the beam, where both polarization components are present. Some studies have explored the distribution of polarization states on the PS [12,59]; however, they do not address their spatial distribution across the transverse plane of the beam.

5. DISCUSSION

There are several mechanisms by which the concurrence of an initially pure state with maximum nonseparability could decay, but perhaps the most prominent in the context of spatial modes is an evolution toward a mixed state (by interacting with an open system, for example) or by modal scattering and subsequent subspace concatenation (ignoring the full expansion in the vector space and considering only the initial subspace). Neither happens here. Instead, our carefully constructed example highlights the counterintuitive dynamics at play: the local concurrence changes dramatically with propagation, eventually decreasing to zero everywhere; yet the global concurrence remains unchanged with propagation, consistent with the fact that free space is a unitary channel, and thus the state vector remains pure, i.e., there is no evolution to a mixed state and no modal scattering. Colloquially, it appears as if the initial beam is split into two homogeneously polarized parts, and so appears separable, it yet remains fully nonseparable in our Hilbert space, as it remains one coherent mode. Our work suggests the need for new or adapted parameters to quantify the nonhomogeneous distribution of polarization states for vector beams. It is intriguing to wonder if our test case may be viewed as a Young's experiment in reverse, with our initial beam mimicking interference to the final beam reminiscent of two slits. Further, this interesting behavior may benefit from recent insights into polarization coherence, where an exact equality linking concurrence, visibility, and duality has been obtained [4]. These and other open questions are exciting challenges for follow-up work.

6. CONCLUSIONS

In this work we demonstrated a novel kind of complex light field that upon free-space propagation evolves from maximally mixed and locally nonseparable to completely unmixed and locally separable. More precisely, we generated a vector beam with a nonhomogeneous polarization distribution that upon free-space propagation evolves into a homogeneously polarized mode. Such behavior is directly observed at various propagation distances through a reconstruction of the transverse polarization distribution performed via Stokes polarimetry. This is further evinced by mapping the entire polarization distribution at each plane onto the Poincaré sphere, which exhibits an evolution of the state of polarization from the equator to the poles. Such evolution happens along spirals connecting the north and south poles. A quantification of this free-pace propagation dynamics was performed through the concurrence C, which takes the value $C = 1$ for vector states and $C = 0$ for scalar beams. We noted that a measure of the global concurrence yields a constant value, while when measuring this in smaller sections of the beam, what we called the "local concurrence," it clearly shows a decrease as a function of the propagation distance, reaching the value $C = 0$ in the far field. In other words,

by measuring the local concurrence we observe what appears to be a decay in nonseparability, even though the entire state is coherent and nonseparable. This evinces the need for an alternative definition of that takes into account the local variations of the nonseparability, but this lies beyond the scope of this research. Importantly, the nonseparability dynamics reported here cannot be observed with cylindrical vector beams, as they are an intrinsic property of parabolic vector beams. It is also worth mentioning that the beam's dynamics can be adjusted through the parameter $z_{\max}$, which depends on ω_0 and k_t. Finally, these novel states of light offer a new tool for a wide variety of applications in fields such as optical communications, optical metrology, and optical tweezers, to mention a few.

Funding. Consejo Nacional de Ciencia y Tecnología (PN2016-3140); National Natural Science Foundation of China (61975047).

Acknowledgment. The authors acknowledge fruitful discussions with Prof. Andrea Aiello from the Max Planck Institute.

Disclosures. The authors declare that there are no conflicts of interest related to this paper.

REFERENCES

1. C. Rosales-Guzmán, B. Ndagano, and A. Forbes, "A review of complex vector light fields and their applications," J. Opt. **20**, 123001 (2018).
2. F. Gori, M. Santarsiero, and R. Borghi, "Vector mode analysis of a young interferometer," Opt. Lett. **31**, 858–860 (2006).
3. J. Eberly, "Shimony–wolf states and hidden coherences in classical light," Contemp. Phys. **56**, 407–416 (2015).
4. X.-F. Qian, A. Vamivakas, and J. Eberly, "Entanglement limits duality and vice versa," Optica **5**, 942–947 (2018).
5. J. H. Eberly, X.-F. Qian, A. A. Qasimi, H. Ali, M. A. Alonso, R. Gutiérrez-Cuevas, B. J. Little, J. C. Howell, T. Malhotra, and A. N. Vamivakas, "Quantum and classical optics–emerging links," Phys. Scr. **91**, 063003 (2016).
6. Y. Shen, X. Yang, D. Naidoo, X. Fu, and A. Forbes, "Structured ray-wave vector vortex beams in multiple degrees of freedom from a laser," Optica **7**, 820–831 (2020).
7. T. Konrad and A. Forbes, "Quantum mechanics and classical light," Contemp. Phys. **60**, 1–22 (2019).
8. A. Forbes, A. Aiello, and B. Ndagano, "Classically entangled light," in *Progress in Optics* (Elsevier, 2019), pp. 99–153.
9. R. J. C. Spreeuw, "A classical analogy of entanglement," Found. Phys. **28**, 361–374 (1998).
10. X.-F. Qian and J. H. Eberly, "Entanglement and classical polarization states," Opt. Lett. **36**, 4110–4112 (2011).
11. X.-F. Qian, A. N. Vamivakas, and J. H. Eberly, "Emerging connections: classical and quantum optics," Opt. Photon. News **28**, 34–41 (2017).
12. K. H. Kagalwala, G. Di Giuseppe, A. F. Abouraddy, and B. E. Saleh, "Bell's measure in classical optical coherence," Nat. Photonics **7**, 72–78 (2013).
13. B. Ndagano, B. Perez-Garcia, F. S. Roux, M. McLaren, C. Rosales-Guzmán, Y. Zhang, O. Mouane, R. I. Hernandez-Aranda, T. Konrad, and A. Forbes, "Characterizing quantum channels with non-separable states of classical light," Nat. Phys. **13**, 397–402 (2017).
14. E. Toninelli, B. Ndagano, A. Vallés, B. Sephton, I. Nape, A. Ambrosio, F. Capasso, M. J. Padgett, and A. Forbes, "Concepts in quantum state tomography and classical implementation with intense light: a tutorial," Adv. Opt. Photon. **11**, 67–134 (2019).
15. B. Ndagano, I. Nape, M. A. Cox, C. Rosales-Guzmán, and A. Forbes, "Creation and detection of vector vortex modes for classical and quantum communication," J. Lightwave Technol. **36**, 292–301 (2018).
16. G. Milione, M. P. Lavery, H. Huang, Y. Ren, G. Xie, T. A. Nguyen, E. Karimi, L. Marrucci, D. A. Nolan, R. R. Alfano, and A. E. Willner, "4 × 20 Gbit/s mode division multiplexing over free space using vector modes and a *q*-plate mode (de)multiplexer," Opt. Lett. **40**, 1980–1983 (2015).
17. Y. Zhao and J. Wang, "High-base vector beam encoding/decoding for visible-light communications," Opt. Lett. **40**, 4843–4846 (2015).
18. X.-B. Hu, B. Zhao, Z.-H. Zhu, W. Gao, and C. Rosales-Guzmán, "*In situ* detection of a cooperative target's longitudinal and angular speed using structured light," Opt. Lett. **44**, 3070–3073 (2019).
19. F. Töppel, A. Aiello, C. Marquardt, E. Giacobino, and G. Leuchs, "Classical entanglement in polarization metrology," New J. Phys. **16**, 073019 (2014).
20. S. Berg-Johansen, F. Töppel, B. Stiller, P. Banzer, M. Ornigotti, E. Giacobino, G. Leuchs, A. Aiello, and C. Marquardt, "Classically entangled optical beams for high-speed kinematic sensing," Optica **2**, 864–868 (2015).
21. V. Shvedov, A. R. Davoyan, C. Hnatovsky, N. Engheta, and W. Krolikowski, "A long-range polarization-controlled optical tractor beam," Nat. Photonics **8**, 846–850 (2014).
22. N. Bhebhe, C. Rosales-Guzmán, and A. Forbes, "Classical and quantum analysis of propagation invariant vector flat-top beams," Appl. Opt. **57**, 5451–5458 (2018).
23. N. Bhebhe, P. A. C. Williams, C. Rosales-Guzmán, V. Rodriguez-Fajardo, and A. Forbes, "A vector holographic optical trap," Sci. Rep. **8**, 17387 (2018).
24. Y. Kozawa and S. Sato, "Optical trapping of micrometer-sized dielectric particles by cylindrical vector beams," Opt. Express **18**, 10828–10833 (2010).
25. S. E. Skelton, M. Sergides, R. Saija, M. A. Iatì, O. M. Maragó, and P. H. Jones, "Trapping volume control in optical tweezers using cylindrical vector beams," Opt. Lett. **38**, 28–30 (2013).
26. M. G. Donato, S. Vasi, R. Sayed, P. H. Jones, F. Bonaccorso, A. C. Ferrari, P. G. Gucciardi, and O. M. Maragó, "Optical trapping of nanotubes with cylindrical vector beams," Opt. Lett. **37**, 3381–3383 (2012).
27. B. Roxworthy and K. Toussaint, "Optical trapping with π-phase cylindrical vector beams," New J. Phys. **12**, 073012 (2010).
28. M. Kraus, M. A. Ahmed, A. Michalowski, A. Voss, R. Weber, and T. Graf, "Microdrilling in steel using ultrashort pulsed laser beams with radial and azimuthal polarization," Opt. Express **18**, 22305–22313 (2010).
29. P. Török and P. Munro, "The use of Gauss-Laguerre vector beams in STED microscopy," Opt. Express **12**, 3605–3617 (2004).
30. X. Hao, C. Kuang, T. Wang, and X. Liu, "Effects of polarization on the de-excitation dark focal spot in STED microscopy," J. Opt. **12**, 115707 (2010).
31. S. Segawa, Y. Kozawa, and S. Sato, "Resolution enhancement of confocal microscopy by subtraction method with vector beams," Opt. Lett. **39**, 3118–3121 (2014).
32. I. Moreno, J. A. Davis, M. M. Sánchez-López, K. Badham, and D. M. Cottrell, "Nondiffracting Bessel beams with polarization state that varies with propagation distance," Opt. Lett. **40**, 5451–5454 (2015).
33. S. Fu, S. Zhang, and C. Gao, "Bessel beams with spatial oscillating polarization," Sci. Rep. **6**, 30765 (2016).
34. J. A. Davis, I. Moreno, K. Badham, M. M. Sánchez-López, and D. M. Cottrell, "Nondiffracting vector beams where the charge and the polarization state vary with propagation distance," Opt. Lett. **41**, 2270–2273 (2016).
35. P. Li, Y. Zhang, S. Liu, H. Cheng, L. Han, D. Wu, and J. Zhao, "Generation and self-healing of vector Bessel-Gauss beams with variant state of polarizations upon propagation," Opt. Express **25**, 5821–5831 (2017).
36. P. Li, D. Wu, Y. Zhang, S. Liu, Y. Li, S. Qi, and J. Zhao, "Polarization oscillating beams constructed by copropagating optical frozen waves," Photon. Res. **6**, 756–761 (2018).
37. P. Li, Y. Zhang, S. Liu, L. Han, H. Cheng, F. Yu, and J. Zhao, "Quasi-Bessel beams with longitudinally varying polarization state generated

by employing spectrum engineering," Opt. Lett. **41**, 4811–4814 (2016).
38. E. Otte, C. Rosales-Guzmán, B. Ndagano, C. Denz, and A. Forbes, "Entanglement beating in free space through spin-orbit coupling," Light Sci. Appl. **7**, 18009 (2018).
39. M. A. Bandres, J. C. Gutiérrez-Vega, and S. Chávez-Cerda, "Parabolic nondiffracting optical wave fields," Opt. Lett. **29**, 44–46 (2004).
40. C. López-Mariscal, M. A. Bandres, J. C. Gutiérrez-Vega, and S. Chávez-Cerda, "Observation of parabolic nondiffracting optical fields," Opt. Express **13**, 2364–2369 (2005).
41. M. A. Bandres, "Accelerating parabolic beams," Opt. Lett. **33**, 1678–1680 (2008).
42. B. M. Rodrguez-Lara and R. Jáuregui, "Dynamical constants of structured photons with parabolic-cylindrical symmetry," Phys. Rev. A **79**, 055806 (2009).
43. A. Ruelas, S. Lopez-Aguayo, and J. C. Gutiérrez-Vega, "Engineering parabolic beams with dynamic intensity profiles," J. Opt. Soc. Am. A **30**, 1476–1483 (2013).
44. J. C. Gutiérrez-Vega and M. A. Bandres, "Helmholtz–Gauss waves," J. Opt. Soc. Am. A **22**, 289–298 (2005).
45. M. McLaren, T. Konrad, and A. Forbes, "Measuring the nonseparability of vector vortex beams," Phys. Rev. A **92**, 023833 (2015).
46. A. Selyem, C. Rosales-Guzmán, S. Croke, A. Forbes, and S. Franke-Arnold, "Basis-independent tomography and nonseparability witnesses of pure complex vectorial light fields by Stokes projections," Phys. Rev. A **100**, 063842 (2019).
47. A. Manthalkar, I. Nape, N. T. Bordbar, C. Rosales-Guzmán, S. Bhattacharya, A. Forbes, and A. Dudley, "All-digital stokes polarimetry with a digital micromirror device," Opt. Lett. **45**, 2319–2322 (2020).
48. B. Zhao, X.-B. Hu, V. Rodríguez-Fajardo, A. Forbes, W. Gao, Z.-H. Zhu, and C. Rosales-Guzmán, "Determining the non-separability of vector modes with digital micromirror devices," Appl. Phys. Lett. **116**, 091101 (2020).
49. B. Ndagano, H. Sroor, M. McLaren, C. Rosales-Guzmán, and A. Forbes, "Beam quality measure for vector beams," Opt. Lett. **41**, 3407–3410 (2016).
50. F. Olver, D. Lozier, R. Boisvert, and C. Clark, and National Institute of Standards and Technology (U.S.), *NIST Handbook of Mathematical Functions Hardback and CD-ROM* (Cambridge University, 2010).
51. C. Rosales-Guzmán, N. Bhebhe, and A. Forbes, "Simultaneous generation of multiple vector beams on a single SLM," Opt. Express **25**, 25697–25706 (2017).
52. C. Rosales-Guzmán, X.-B. Hu, A. Selyem, P. Moreno-Acosta, S. Franke-Arnold, R. Ramos-Garcia, and A. Forbes, "Polarisation-insensitive generation of complex vector modes from a digital micromirror device," Sci. Rep. **10**, 10434 (2020).
53. Y. Li, X.-B. Hu, B. Perez-Garcia, B. Zhao, W. Gao, Z.-H. Zhu, and C. Rosales-Guzmán, "Classically entangled Ince–Gaussian modes," Appl. Phys. Lett. **116**, 221105 (2020).
54. D. H. Goldstein, *Polarized Light* (CRC Press, 2011).
55. B. Zhao, X.-B. Hu, V. Rodríguez-Fajardo, Z.-H. Zhu, W. Gao, A. Forbes, and C. Rosales-Guzmán, "Real-time Stokes polarimetry using a digital micromirror device," Opt. Express **27**, 31087–31093 (2019).
56. J. W. Goodman, *Introduction to Fourier Optics*, 4th ed. (WH Freeman, 2017).
57. S. Scholes, R. Kara, J. Pinnell, V. Rodríguez-Fajardo, and A. Forbes, "Structured light with digital micromirror devices: a guide to best practice," Opt. Eng. **59**, 041202 (2019).
58. S. Yang, S. A. Ponomarenko, and Z. D. Chen, "Coherent pseudo-mode decomposition of a new partially coherent source class," Opt. Lett. **40**, 3081–3084 (2015).
59. P. Réfrégier, "Polarization degree of optical waves with non-Gaussian probability density functions: Kullback relative entropy-based approach," Opt. Lett. **30**, 1090–1092 (2005).